GDCh Research Article Angewandte International Edition Chemie www.angewandte.org

How to cite: *Angew. Chem. Int. Ed.* **2025**, e202505372
doi.org/10.1002/anie.202505372

Batteries

Molecularly Engineered Circular Additive with Multisite Desolvation for High-Performance Zinc Ion Battery

Jinliang Yan, Haozhen Dou, Mengke Su, Mi Xu, Sitong Liu, Siqi Qin, Beinuo Zhang, Kai Zong, Lichao Tan, Xin Wang,* and Zhongwei Chen**

Abstract: Additive engineering can effectively relieve interface issues of aqueous zinc ion batteries (AZIBs), but most additives induce the sluggish interface kinetics and boosted polarization, especially at high current density and low temperature. Herein, the relationship between additive molecular structure and desolvation behavior is built by utilizing a series of circular and linear sugar molecules as prototypes, which systematically reveals molecular size, steric configuration, and electronic structure as design criteria for additives to achieve fast desolvation. As indicated by theoretical simulations and experiments, circular fructose (FRU) molecule with small size, quasi-planar adsorption configuration, and enhanced electron delocalization enables the compact electric double layer (EDL) with shorter Zn^{2+} diffusion path and lower activation energy via multisite desolvation, thus obtaining the rapid interface kinetics and facilitating highly reversible zinc anode over a wide temperature range. Zn//Zn cell exhibits long cycle life exceeding 9500 h, and Zn//NVO cell maintains 83.92% high-capacity retention after 2480 cycles under 6.95 μL mg^{-1} lean electrolyte and 11.94 mg cm^{-2} high loading.

Introduction

Aqueous zinc ion batteries (AZIBs) represent a promising energy storage technology that is capable of efficiently storing intermittent renewable energy sources. AZIBs were expected to replace traditional lead-acid batteries and complement lithium-ion batteries for large-scale energy storage due to low cost and high safety.[1–5] However, the hydrated $[Zn(H_2O)_6]^{2+}$ solvation structure results in water-rich electric double layer (EDL) with abundant thermodynamically active H_2O molecules, which induces interfacial parasitic reactions of hydrogen evolution reaction (HER) and corrosion.[6–9] The parasitic reactions bring uneven distribution of interfacial electric field, which causes the inhomogeneous Zn^{2+} deposition and accelerates dendrite growth. Moreover, the strong dipolar Zn^{2+} interaction within solvation shell induces the slow desolvation with high energy barrier, which further exacerbates the interfacial issues (Figure 1a), thus significantly reducing the cycle life.[10–12]

Versatile strategies such as constructing protective layer and nanostructured host have been proposed to solve the above challenges. Among the proposed solutions, electrolyte additive engineering is a straightforward and effective strategy, offering the advantages of facile operation and notable cost-effectiveness. Functional additives have been introduced into aqueous electrolytes for tailoring solvation structure or/and interface chemistry to improve battery performance.[13–17] Remarkably, sacrificial-type additives are widely explored to in situ construct the solid electrolyte interface (SEI) for inhibiting HER and dendrite growth. However, the continuous consumption of additives results in the limited enhancement of battery performance during long-term cycling.[18–21] Alternatively, nonsacrificial-type additives deliver the dynamic and durable regulation capacity, which has aroused intensive research interest. Some organic solvents or solutes may replace H_2O molecules in Zn^{2+} solvation shell or confine H_2O molecule via hydrogen-bond network reconstruction, which reduces the H_2O activity and suppresses parasitic reactions.[22–26] In addition, certain nonsacrificial additives with large molecular weights spontaneously adsorb on the zinc anode surface via interactions between their polar groups (e.g., carboxyl groups, amino groups) and metal anode, which can effectively manipulate Zn^{2+} diffusion and hinder the dendrite growth.[27–29] Despite the great progress, the modification effectiveness of additives highly depends on the high concentration or strong coordination between additive and zinc anode (or Zn^{2+}), which results in formidable desolvation and sluggish interface kinetics, thus causing high polarization overpotential and poor cycle life under high current density or low temperature. Moreover, some organic additives compromise low cost and high safety of AZIBs.[30–33] Therefore, it is imperative to gain a comprehensive

[*] J. Yan, M. Su, S. Liu, K. Zong, L. Tan, Prof. X. Wang
Institute of Carbon Neutrality, Zhejiang Wanli University, Ningbo 315100, China
E-mail: wangx@zwu.edu.cn
wangxin@scnu.edu.cn

J. Yan, M. Su, S. Liu, Prof. X. Wang
South China Academy of Advanced Optoelectronics, South China Normal University, Guangzhou 510006, China

Prof. H. Dou, M. Xu, S. Qin, B. Zhang, Prof. Z. Chen
Power Battery and Systems Research Center, State Key Laboratory of Catalysis, Dalian Institute of Chemical Physics, Chinese Academy of Science Dalian, Dalian 116023, China
E-mail: haozhen@dicp.ac.cn
zwchen@dicp.ac.cn

Additional supporting information can be found online in the Supporting Information section

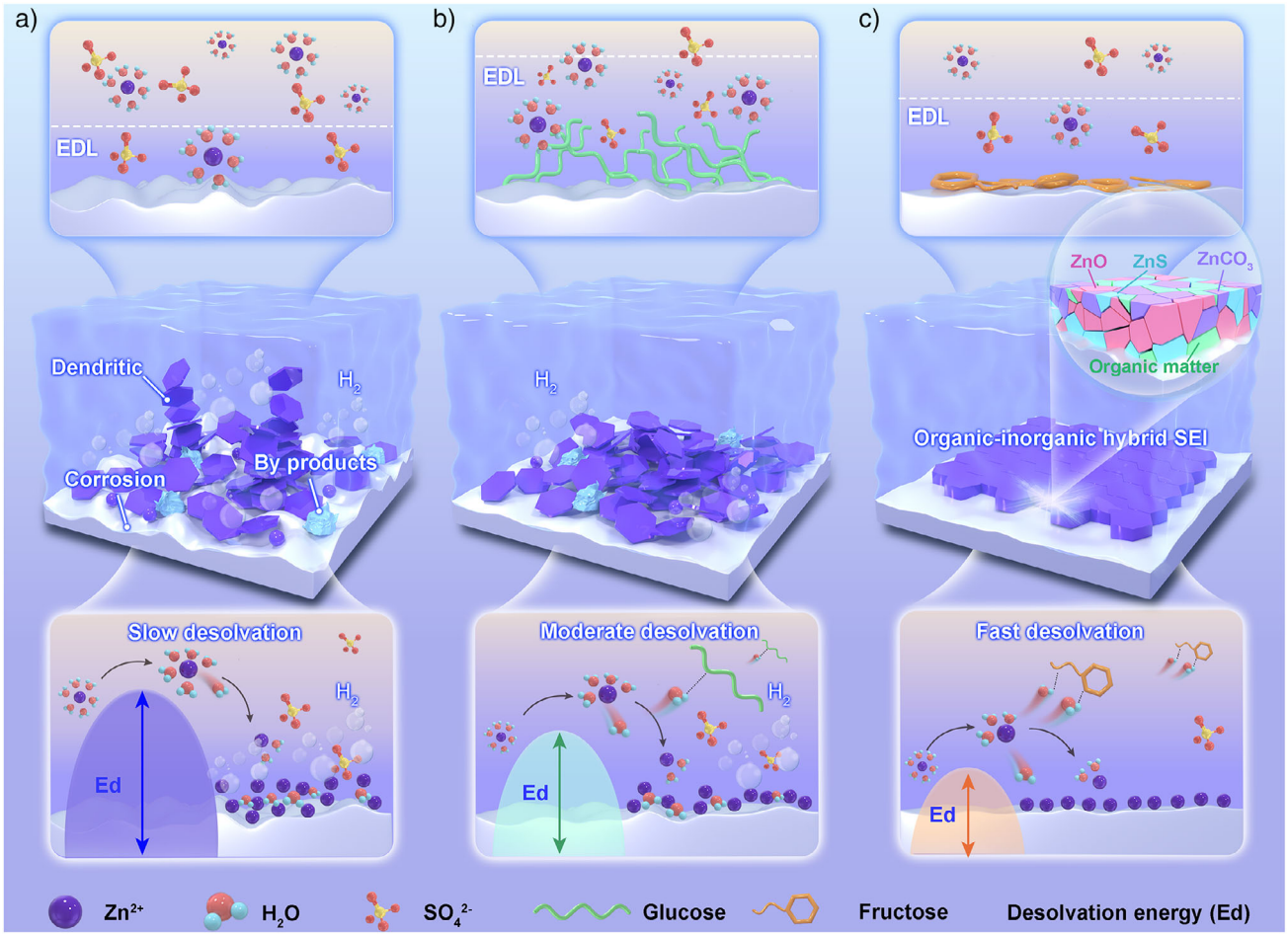

Figure 1. Molecular engineering of electrolyte additives regulates Zn^{2+} desolvation kinetics and interfacial evolution. a) Baseline scenario in $ZnSO_4$ (ZS) electrolyte: the solvated $[Zn(H_2O)_6]^{2+}$ complexes induce EDL, triggering parasitic HER, zinc corrosion, and dendritic growth through inhomogeneous Zn^{2+} deposition. b) Linear GLU molecules partially suppress HER by reconstructing the hydrogen-bond network, but their vertical adsorption configuration results in insufficient interfacial coverage, allowing residual dendrite propagation. c) Circular FRU molecules with quasi-planar adsorbed configuration and electron delocalization characteristics enable multisite coordination, effectively weakening the binding energy of $[Zn(H_2O)_6]^{2+}$. Through in situ interfacial reactions, a compact organic–inorganic hybrid SEI is formed, which reduces the EDL thickness and achieves homogeneous Zn^{2+} flux distribution.

understanding of the relationship between additive molecule structure and interface kinetics, and developing safe additives to obtain high battery performance in harsh conditions and building the rational design criteria for additives are highly desirable.[34,35]

Biomolecules, such as proteins, amino acids, and sugars, have attributes of wide availability, high safety, and biodegradability, which have been widely developed as electrolyte additives for AZIBs.[36–38] Particularly, sugar molecules exhibit structural diversity with significant variation in molecule size and configuration, which makes them an ideal material platform for revealing the structure-performance relationship of electrolyte additives. In this study, a series of circular and linear sugar molecules, including fructose (FRU), glucose (GLU), maltose (MAL), and sucrose (SUC), are selected as prototypes, and the effects of their molecular structure on interface kinetics and electrochemical performance are systematically investigated. As indicated by theoretical simulations and experiments, molecular size, steric configuration, and electronic structure of additives are the decisive factors for achieving fast desolvation. Compared with linear molecule or large-sized molecule, circular FRU molecule with small size, quasi-planar adsorption configuration, and enhanced electron delocalization enables the compact EDL with shorter Zn^{2+} diffusion path and lower activation energy via multisite desolvation, thus obtaining the rapid interface kinetics (Figure 1b,c). In addition, FRU can effectively modulate the Zn^{2+} solvation structure and interfacial chemistry, thereby contributing to the dense dendrite-free Zn deposition and significantly enhancing the reversibility of zinc anode under wide temperature. In symmetric cells, the electrolyte containing FRU demonstrates a stable cycling capability of 9500 h at a current density of 0.5 mA cm^{-2}. The Zn//NVO full cell delivers a high-capacity retention of 83.92% over 2480 cycles at lean electrolyte of 6.95 µL mg^{-1} and a high mass loading of 11.94 mg cm^{-2}. This study established, for the first time, a clear correlation between additive molecule structure and interface desolvation kinetics, which provides

a new prospect for designing high-performance AZIBs via structure customization of additives.

Results and Discussion

Correlation Between Molecule Structure and Desolvation Kinetics

To elucidate the relationship between molecule structure and desolvation behavior, four circular and linear sugar molecules with varied size and configuration were selected as additives and a family of electrolytes was formulated by incorporating these sugar molecules into a 2 M $ZnSO_4$ (ZS) aqueous electrolyte at molar ratio of 4:1, denoted as FRU-41, GLU-41, MAL-41, and SUC-41 (Figure S1). Given the excellent compatibility of sugars with H_2O, all prepared electrolytes remained clear, transparent, and stable. Figures 2a and S2 compared the rate performance of Zn//Zn symmetric cells with different electrolytes at current densities varying from 0.5 to 10 mA cm^{-2}, suggesting that polarization overpotential was significantly affected by additive molecule structure. As highlighted in Figure 2b, the overpotential exhibited a consistent trend across different current densities, with the order following FRU-41 < GLU-41 < MAL-41 < SUC-41. Notably, FRU-41, containing the circular FRU molecule, exhibited the lowest polarization, with an overpotential of only 89.9 mV even at high current density of 10 mA cm^{-2} (Table S1). Undoubtedly, Zn^{2+} exists as the highly hydrated $[Zn(H_2O)_6]^{2+}$ complex in aqueous electrolyte, and desolvation is often the rate-determining step in electrochemical reactions.[10,39] Therefore, the increase in overpotential could have originated from the sluggish desolvation process at the electrode/electrolyte interface. The desolvation behavior was investigated at different temperatures using electrochemical impedance spectroscopy (EIS; Figures 2c and S3),[40,41] and the activation energy (E_a) obtained via Arrhenius equation fitting follows the trend FRU-41 < GLU-41 < MAL-41 < SUC-41, and its values indirectly reflect the trend of desolvation energy (E_d), consistent with the mechanistic role of desolvation as the rate-determining step. FRU-41 exhibited a notably lower E_a (21.93 kJ mol^{-1}), while values for GLU-41, MAL-41, SUC-41, and ZS reach 32.09, 35.11, 35.24, and 41.51 kJ mol^{-1} (Figure 2d). As anticipated, a distinct positive correlation was observed between E_d and overpotential polarization.

Density functional theory (DFT) calculations were performed to reveal the molecule structure of these sugar additives, including molecular size, electrostatic potential (ESP), and electron delocalization, which helpfully built the relationship between molecular structure and desolvation kinetics.[42–45] The molecule size of sugar additives followed the trend of FRU < GLU < MAL < SUC (Table S2 and Figure S4), suggesting that larger molecular sizes led to slower desolvation. The ESP of sugar molecules confirmed the abundant positive and negative charged sites, which allows them to act as both hydrogen-bond donors and hydrogen-bond acceptors (Figure 2e), thus modulating electrolyte property.[10,38] Significantly, the ESP range (maximum to minimum charge) of SUC, MAL, and GLU was considerably larger than that of FRU (Table S3 and Figure S5). The expanded ESP range correlated with the stronger Zn^{2+} interactions and increased steric hindrance, resulting in slower desolvation.[46–48] Moreover, the electronic delocalization of additives aligned with the measured E_a values. Particularly, compared with linear GLU, circular FRU exhibited the enhanced electronic delocalization and a more homogeneous charge distribution (Figure 2f), leading to more rapid and uniform Zn^{2+} desolvation.[49] Although the desolvation process of Zn^{2+} was severely hindered at low temperatures, the cyclic molecules still enable symmetric cells to achieve the lowest polarization and longest cycle lifespan (Figure 2g). Therefore, molecule size and electronic structure were decisive factors for desolvation kinetics, and circular molecules with small size and enhanced electron delocalization enabled the most favorable desolvation behavior.

Intermolecular Forces and Solvation Structure

In light of the superior performance of FRU, a series of FRU electrolytes with varying $ZnSO_4$/FRU molar ratios were formulated, which were donated as FRU-41, FRU-21, FRU-11, and FRU-12 (Figure S6). FRU electrolytes maintained high safety as confirmed by ignition testing (Figure S7). More importantly, the abundant hydrogen bond donor and acceptor sites of FRU molecule effectively modulated the hydrogen bond network of electrolyte,[47,50,51] thereby expanding its operating-temperature range. Antifreeze experiments and volatility tests (Figures S8 and S9) demonstrated that FRU electrolytes remained in a liquid state at temperature of −20 °C, and effectively suppressed volatility at 60 °C during 10 h test. Although the ionic conductivity of FRU electrolytes decreased slightly with the introduction of FRU (Figure S10), it remained at a high level, far exceeding that of organic solvent electrolytes. Encouragingly, FRU effectively enhanced Zn^{2+} transfer number, boosting from 0.171 to 0.670 (Figures 3a and S11), which promoted uniform Zn^{2+} diffusion and fast kinetics.[52,53]

Density functional theory calculation, ^1H NMR, Fourier transform infrared spectroscopy (FTIR), and Raman analyses were performed to investigate the intermolecular interactions of FRU electrolyte. As revealed by DFT calculation, FRU molecule exhibited the stronger interaction with Zn^{2+} via highly electronegative O atom of O–H group compared with H_2O (−114.33 kcal mol^{-1}), suggesting its grand possibility for regulating the solvation structure (Figure 3b).[53,54] Concurrently, the hydrogen bond interaction between SO_4^{2-} (or FRU) and H_2O is stronger than that between H_2O molecules, thereby facilitating the reconstruction of the hydrogen-bond network. ^1H NMR spectra indicated that the chemical shift of H_2O shifted to up-field and gradually weakened (Figure 3c), suggesting that the intermolecular hydrogen bonds of H_2O were disrupted, thus reducing thermodynamic activity of H_2O.[55–57] The hydrogen bond environment of H_2O was further analyzed by FTIR (Figures 3d,e and S12). The observed blue shift of the stretching vibration peak (3200–3600 cm^{-1}) for H_2O molecules in the FRU-11 confirmed the formation

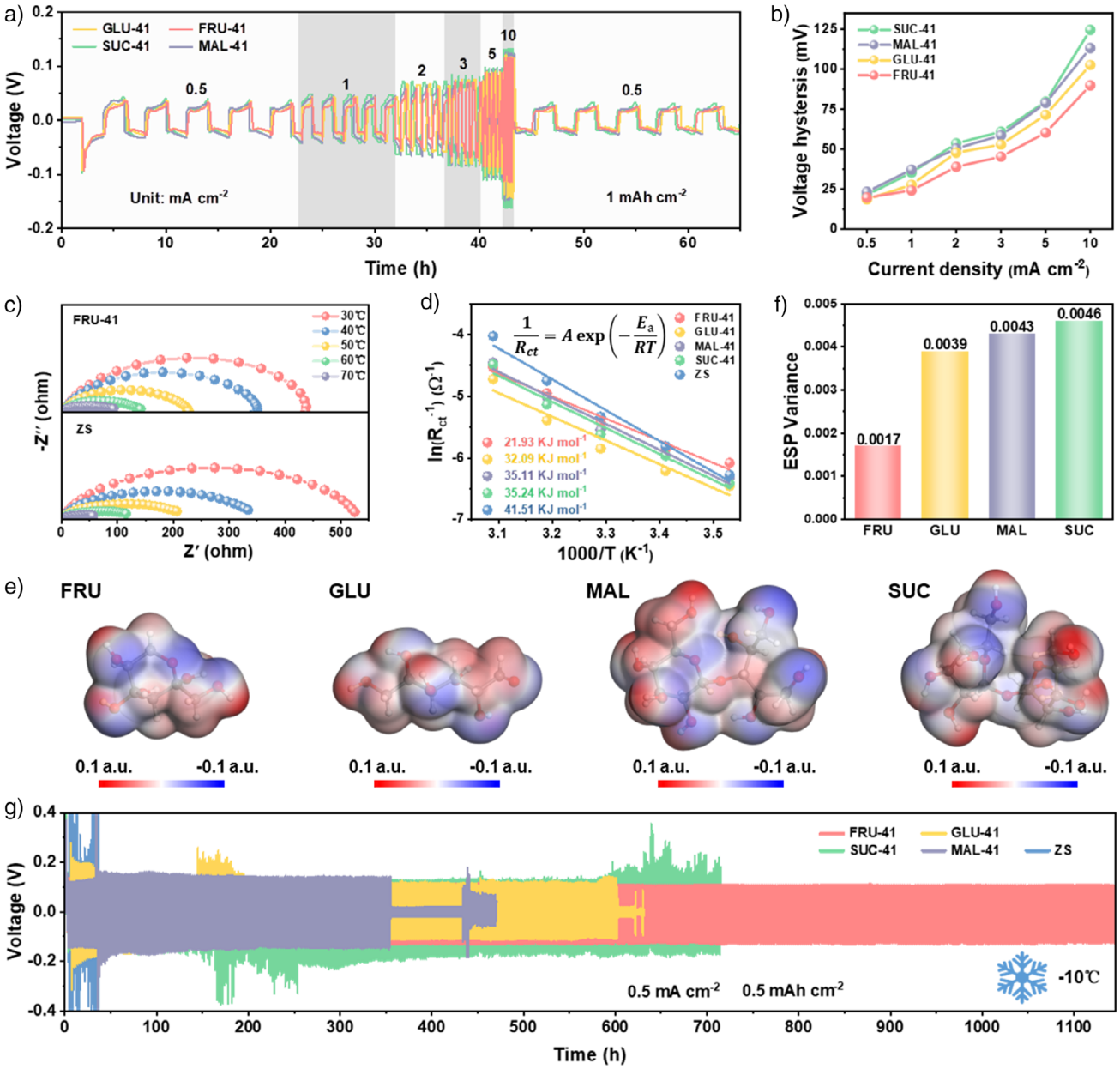

Figure 2. Desolvation behavior studies. a) Effect of different sugar additives on the multiplicity performance of Zn//Zn symmetric cells. b) Comparison of overpotential of each electrolyte at different current densities. c) EIS of FRU-11 and ZS symmetric cells in the temperature range of 30–70 °C. d) Comparison of Arrhenius curves and activation energies of different sugar electrolytes. e) Electrostatic potential distribution of different sugar molecules. f) Comparison of inhomogeneity of electron cloud distribution around nuclei of different sugar molecules. g) Time–voltage curves of symmetric cells with different sugar electrolytes at −10 °C.

of intermolecular hydrogen bonds between FRU and H_2O molecules.[58,59] Additionally, the stretching vibration peak of SO_42^- exhibited a significant red shift, with the degree of red shift in proportion to the concentration of FRU. This phenomenon was attributed to the weakened electrostatic interactions between SO_42^- and Zn^{2+}, which facilitated the Zn^{2+} diffusion and transport. Raman spectroscopic analysis corroborated these findings (Figure S13), similarly revealing significant alterations in the hydrogen bonds and electrostatic interactions.[60,61]

The type and number of intermolecular hydrogen bonds were further investigated through molecular dynamics (MD) simulations (Figure 3f). Compared to ZS, the total number of hydrogen bonds in FRU-11 increased from 17 800 to about 18 700.[62] A closer examination of the hydrogen bond composition ratio revealed a 14.89% reduction in the number of hydrogen bonds between H_2O molecules (Figures 3g and S14). Concurrently, new types of hydrogen bonds have been formed between FRU molecules, H_2O molecules, and SO_42^-. More importantly, Zn^{2+} solvation structure was further

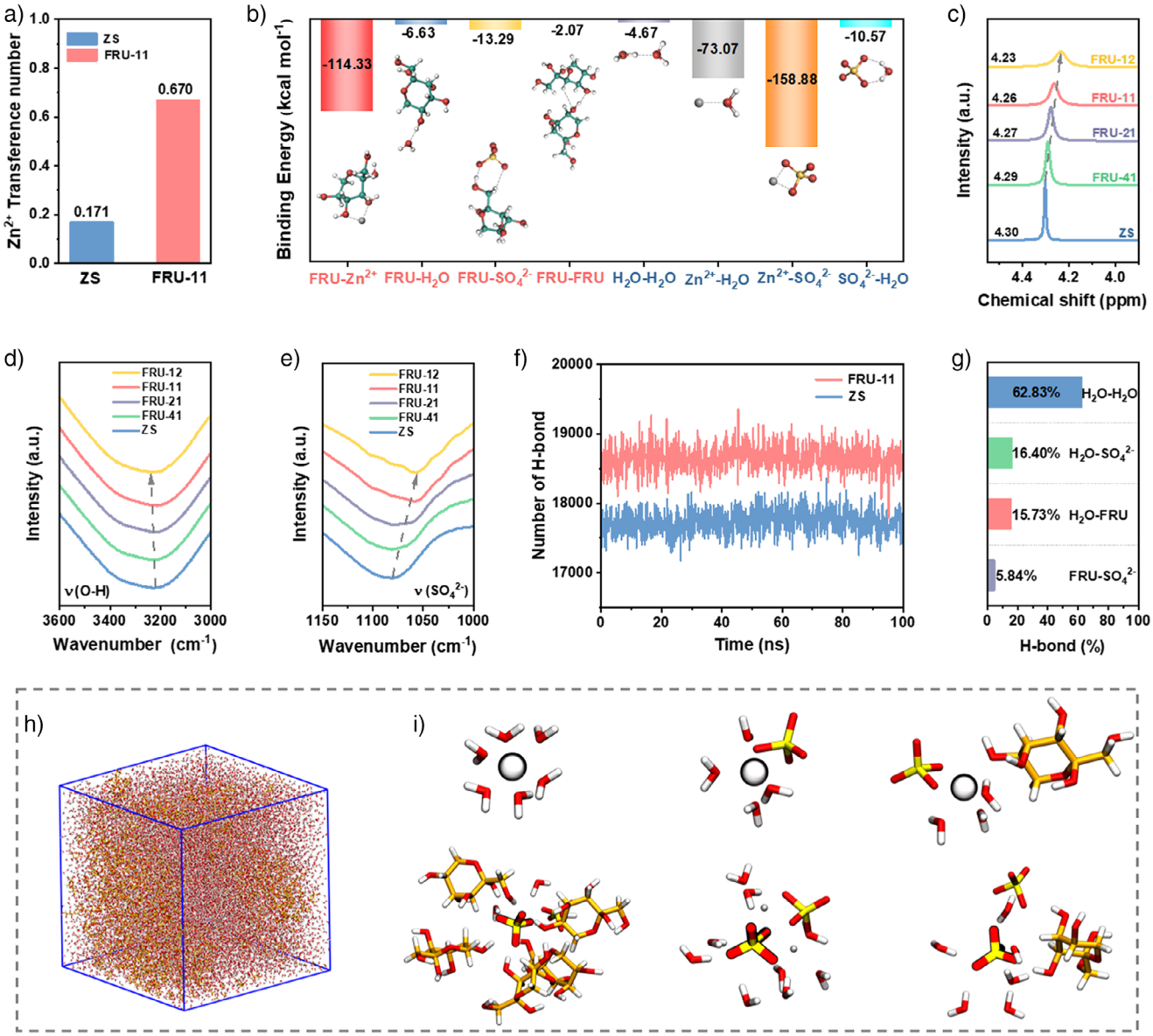

Figure 3. Structural characteristics of the FRU electrolyte. a) Comparison of Zn^{2+} transference numbers in ZS and FRU-11 electrolytes. b) Interaction energies between components in FRU-11 calculated by DFT. c) ^{1}H NMR spectra of different electrolytes. d) and e) FTIR spectra. f) Number of hydrogen bonds in FRU-11 and ZS systems obtained from MD simulations. g) Types and proportions of hydrogen bonds in FRU-11. h) MD simulation snapshot of FRU-11. i) Coordination environments of Zn^{2+} and SO_4^{2-} in FRU-11 from MD simulations.

provided by MD simulations (Figure 3h,i). The solvation environments of Zn^{2+} and SO_42^{-} were significantly altered by the introduction of FRU. Radial distribution function (RDF) and coordination number (CN) analysis indicated that Zn^{2+} primary solvation shell (PSS) in ZS was predominantly formed with 5.3 H_2O and 0.7 SO_4^{2-} (Figure S15). In FRU-11, the solvation environment was modified, with the PSS of Zn^{2+} now comprising 4.9 H_2O molecules, 0.7 FRU molecules, and 0.4 SO_4^{2-}.[49,63] Furthermore, the nanocluster morphology of the electrolyte was modified by the presence of FRU (Figures S1 and S18), which resulted in a more uniform distribution of Zn^{2+} and enhanced ionic conductivity, being consistent with previously reported findings.[62]

Compact EDL and Multisite Desolvation

Adsorption behavior of FRU molecule at the interface, as well as the EDL structure and desolvation mechanism, were investigated by a combination of DFT calculations and experimental studies. DFT calculations revealed the adsorption behavior of H_2O, circular FRU, and linear GLU molecules on the Zn(002) crystal plane (Figures 4a and S19). The additive molecules exhibited higher adsorption energy toward the zinc anode than that of H_2O molecule, which confirmed their preferential adsorption to reduce interfacial H_2O activity for suppressing HER and side reactions. Parallel (P) adsorption exhibited a greater adsorption energy

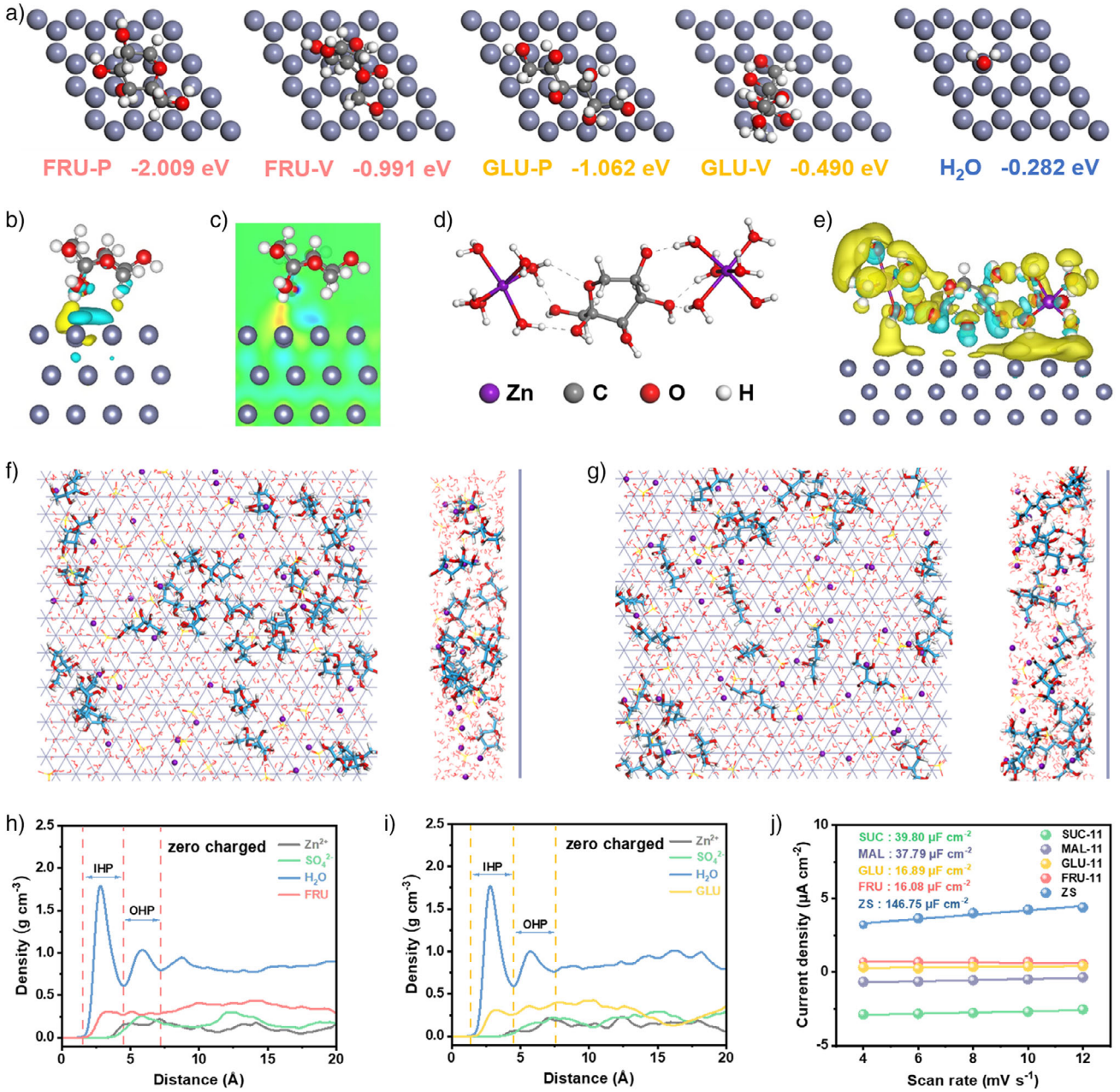

Figure 4. Influence of molecular size and structure on EDL properties at the electrode interface. a) Comparison of adsorption energies of H_2O, FRU, and GLU on Zn(002) crystal surface and their adsorption patterns. b) Distribution of charge density difference along the Z-axis direction after parallel adsorption of FRU molecules on the Zn(002) crystalline surface, with yellow and cyan colors indicating the electron aggregation and deficit regions, respectively. c) Corresponding 2D contour plots of the slices. d) Hydrogen bond interactions between FRU molecules and solvated Zn^{2+} and e) their differential charge density distributions on Zn(002) crystal faces. Top and side views of MD simulation snapshots of the EDL structure formed by f) FRU and g) GLU molecules on the surface of the zinc anode. h) Density distribution of SO_4^{2-}, H_2O, and Zn^{2+} in FRU-11 and i) GLU-11 at zero potential along the direction away from the zinc anode. j) Differential capacitance curves of different structures of sugar-containing electrolyte.

than vertical (V) adsorption for both linear and circular molecules. Consequently, additive molecules preferred to adsorb in a parallel manner at the interface.[49,64] Circular molecules exhibited higher binding energy than linear molecules in both parallel and vertical adsorption, which was attributed to the larger coplanar molecular surface area of circular molecules, facilitating multisite adsorption via quasi-planar adsorption configuration. Multisite adsorption not only increased the surface coverage of additive molecules but also promoted the homogeneous zinc deposition by regulating Zn^{2+} diffusion. Charge density difference distribution and 2D slice visualization further confirmed the electron transfer from FRU to the Zn(002) surface (Figures 4b,c and S20), which occurred from the C—O and O—H bonds of FRU molecule to the zinc anode, thus inducing strong chemisorption. Moreover, the synergistic effect of

multisite charge transfer further enhanced the adsorption strength.[65,66]

Desolvation mechanism of Zn^{2+} was elucidated by DFT calculations based on the multisite parallel adsorption configuration of additive molecule (Figures 4d,e and S21).[10] Using the typical $[Zn(H_2O)_6]^{2+}$ solvation shell, it was found that FRU molecule could form strong hydrogen bonds with the solvated H_2O molecules through multiple sites, thus weakening the coordination between Zn^{2+} and H_2O and facilitating the rapid desolvation of Zn^{2+}. In addition, charge density difference analysis further confirmed the formation of intermolecular hydrogen bonds and the strong interaction between FRU and zinc anode.[49]

Molecular configuration significantly affected EDL structure on the zinc anode. MD simulations indicated that circular FRU molecules tended to adsorb parallel to the electrode surface, forming a dense and compact EDL. Due to this parallel adsorption configuration, FRU molecules readily penetrated the inner Helmholtz plane (IHP), establishing strong interactions with the electrode. These strong interactions allowed FRU molecules to maintain a stable distribution within the IHP at negative, zero, and positive potentials (Figures 4f and S22), effectively hindering water penetration and reducing interfacial water content.[62,67] In contrast, linear GLU molecules exhibited a different adsorption behavior, primarily adopting vertical or tilted orientations at adsorption sites (Figures 4g and S23). The corresponding density distribution profiles further confirmed the distinct adsorption modes. For example, at zero potential, a thinner IHP and outer Helmholtz plane (OHP) were observed for FRU compared to GLU (Figures 4h,i, S24, and 25). The accumulation of FRU in the EDL slightly diminished the wettability of the electrode surfaces (Zn and Ti), and this subtle alteration contributed to the formation of a more stable solid–liquid interface (Figure S26). As further revealed by electric double-layer capacitance (EDLC), the introduction of additives resulted in a decrease in EDLC, suggesting that additive molecules entered the EDL (Figures 4j and S27). As dictated by the relationship $C = \varepsilon A/d$, smaller capacitance corresponds to larger EDL thickness.[68–70] For instance, larger-sized SUC and MAL molecules resulted in greater EDL thicknesses compared to FRU and GLU. Interestingly, the circular FRU molecule exhibited a much lower EDLC compared to linear GLU molecule. This was likely attributed to its quasi-planar adsorption configuration, which minimized the EDL thickness, thereby shortening the mass transport distance and further facilitating faster Zn^{2+} desolvation.

Interface Structure and Chemistry

X-ray photoelectron spectroscopy (XPS), high-resolution transmission electron microscopy (HR-TEM), and time-of-flight secondary ion mass spectrometry (TOF-SIMS) were utilized to investigate the structure and chemistry of SEI on the zinc anode after cycling. XPS survey spectra (Figures S28 and S29) demonstrated the distinct interfacial chemistry between FRU-11 and ZS electrolytes, with FRU-11 exhibiting a stronger Zn signal. As illustrated in Figure 5a, the higher Zn content in the FRU-11 Zn 2p spectrum confirmed a dense SEI. The C 1s spectrum indicated a $ZnCO_3$-rich SEI formed by FRU-11, whose C─C/C─H and C─O components enhanced SEI stability. The O 1s spectra exhibit oxygen signals attributable to $ZnCO_3$, $ZnSO_4$, and organic species, with negligible $Zn(OH)_2$ signals, indicating suppressed side reactions. Furthermore, ZnS observed in the S 2p spectra, which originates from the decomposition of SO_42^- in the electrolyte, further enhances SEI protection.[71] In contrast, the higher Zn^{2+} content observed in the Zn 2p spectrum for ZS was attributed to pronounced side reactions (Figure S30a). Minimal carbon species were detected in the C 1s spectrum, with $ZnCO_3$ nearly absent (Figure S30b). A pronounced $Zn(OH)_2$ signal in the O 1s spectrum further corroborated the occurrence of extensive side reactions (Figure S30c). The S 2p spectrum showed that SO_42^- remained predominant, indicating the plenty of by-product (Figure S30d). Therefore, an organic–inorganic hybrid SEI in in situ formed in FRU electrolyte, which further enhanced interfacial stability.[72,73]

HR-TEM confirmed the structural characteristics of the SEI (Figure 5b). The SEI formed by FRU-11 consisted primarily of crystalline inorganic components, such as $ZnCO_3$ and ZnS, with minor incorporation of amorphous organic components derived from FRU. This structure effectively suppressed interfacial water activity, mitigating HER and side reactions. Uniform elemental distribution was observed in the EDS mapping (Figure 5c).[74,75] In contrast, the SEI formed in ZS was primarily composed of $ZnSO_4$ and $Zn(OH)_2$ and exhibited structural instability, being consistent with the XPS results (Figure S31). The elemental distribution and spatial architecture of SEI were further analyzed by TOF-SIMS (Figures 5d and S32). The cycled zinc anode surface in FRU-11 was enriched with C, S, and O, as well as inorganic components like ZnO and ZnS, facilitating Zn^{2+} migration across the interface and uniform deposition. This observation aligned with the dense SEI model depicted in Figure 5e. Conversely, zinc anode with ZS exhibited significant elemental distribution gradients and pronounced defects, particularly with highly nonuniform distributions of O and S as well as substantial generation of $Zn(OH)_2$ by-product, hindering the formation of an effective SEI.[26,76]

Structural Evolution of Zinc Anode

The structural evolution of zinc anode was investigated through multiscale characterization techniques. The elevated HER overpotential observed in linear sweep voltammetry (LSV) curves (Figure 6a),[62] together with the suppressed H_2 evolution during Zn^{2+} deposition confirmed by differential electrochemical mass spectrometry (DEMS), demonstrated that FRU-11 effectively mitigated free H_2O-induced HER side reactions (Figure S33).[77] This enhancement was attributed to the modulation of the solvation structure by FRU-11 and the formation of a water-deficient EDL at the electrode interface. Scanning electron microscope (SEM) images of zinc anode from the immersion experiment further demonstrated that FRU-11 effectively inhibited self-corrosion, with a dense interface layer serving to block

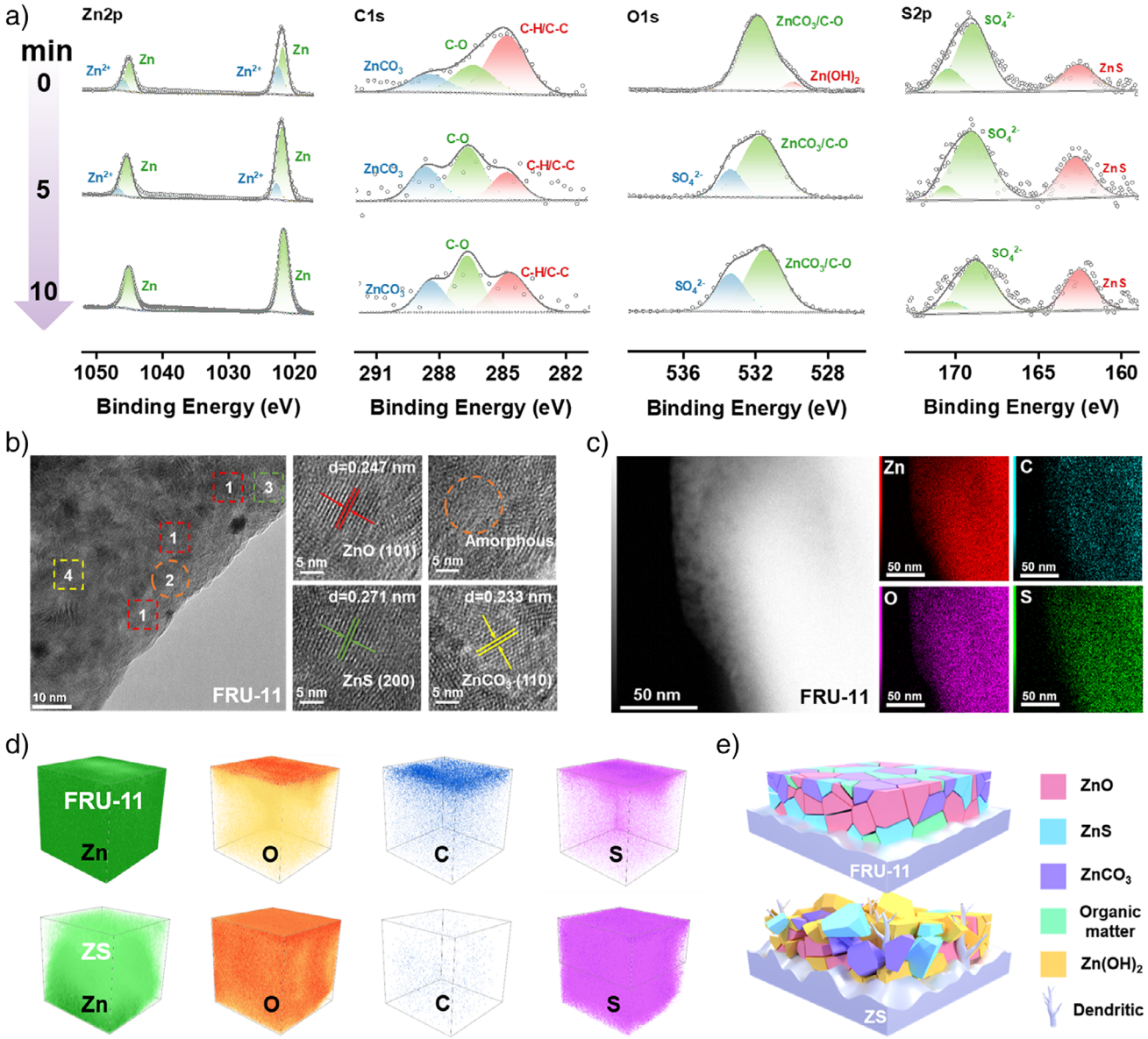

Figure 5. Morphology and chemical composition of the SEI. a) XPS spectra of Zn 2p, C 1s, O 1s, and S 2p for zinc anode cycled in FRU-11 electrolyte for 100 cycles at different etching times. b) HR-TEM image of zinc anode after galvanostatic charging at 1 mA cm^{-2} for 10 min in FRU-11 and c) corresponding TEM-EDS elemental mapping. d) 3D spatial distribution of surface elements of the zinc anode after 100 cycles in different electrolytes via TOF-SIMS. e) Schematic illustration of the SEI composition on the Zn foil surface after cycling in different electrolytes.

electrolyte erosion (Figures 6b and S34). In contrast, the surface roughness of zinc anode immersed in ZS increased significantly, resulting in the formation of numerous holes and cracks. At a current density of 5 mA cm^{-2}, SEM images obtained at various deposition times revealed the distinct differences in Zn^{2+} nucleation process between ZS and FRU-11 (Figure S35). In ZS, uncontrolled zinc deposition resulted in the formation of nuclei with varying sizes, ultimately leading to a porous and dendritic morphology susceptible to short circuits. Conversely, uniform and controlled growth of fine zinc nuclei was observed in FRU-11, effectively preventing dendrite formation.[78] Cyclic voltammetry (CV) curves revealed a higher nucleation overpotential (NOP) for FRU-11 (37.98 mV) (Figure S36). This increased NOP, corresponding to a higher nucleation driving force, facilitated the formation of a large number of smaller grains.[79] Additionally, chronoamperometry (CA) was employed to further analyze the differences in Zn^{2+} deposition behavior (Figure S37). At a constant potential of −150 mV, the current in ZS consistently increased over time, exhibiting a typical 2D diffusion-controlled deposition mode. On the contrary, the current in FRU-11 rapidly stabilized within seconds, suggesting that 2D diffusion of Zn^{2+} was suppressed, resulting in a more uniform deposition process.[80] The morphology of zinc anodes after cycling was observed by SEM (Figures 6c and S38). After 100 cycles, zinc anode surface in ZS exhibited a large number of vertically grown dendrites, while a flat and dense morphology was maintained in FRU-11. Focused

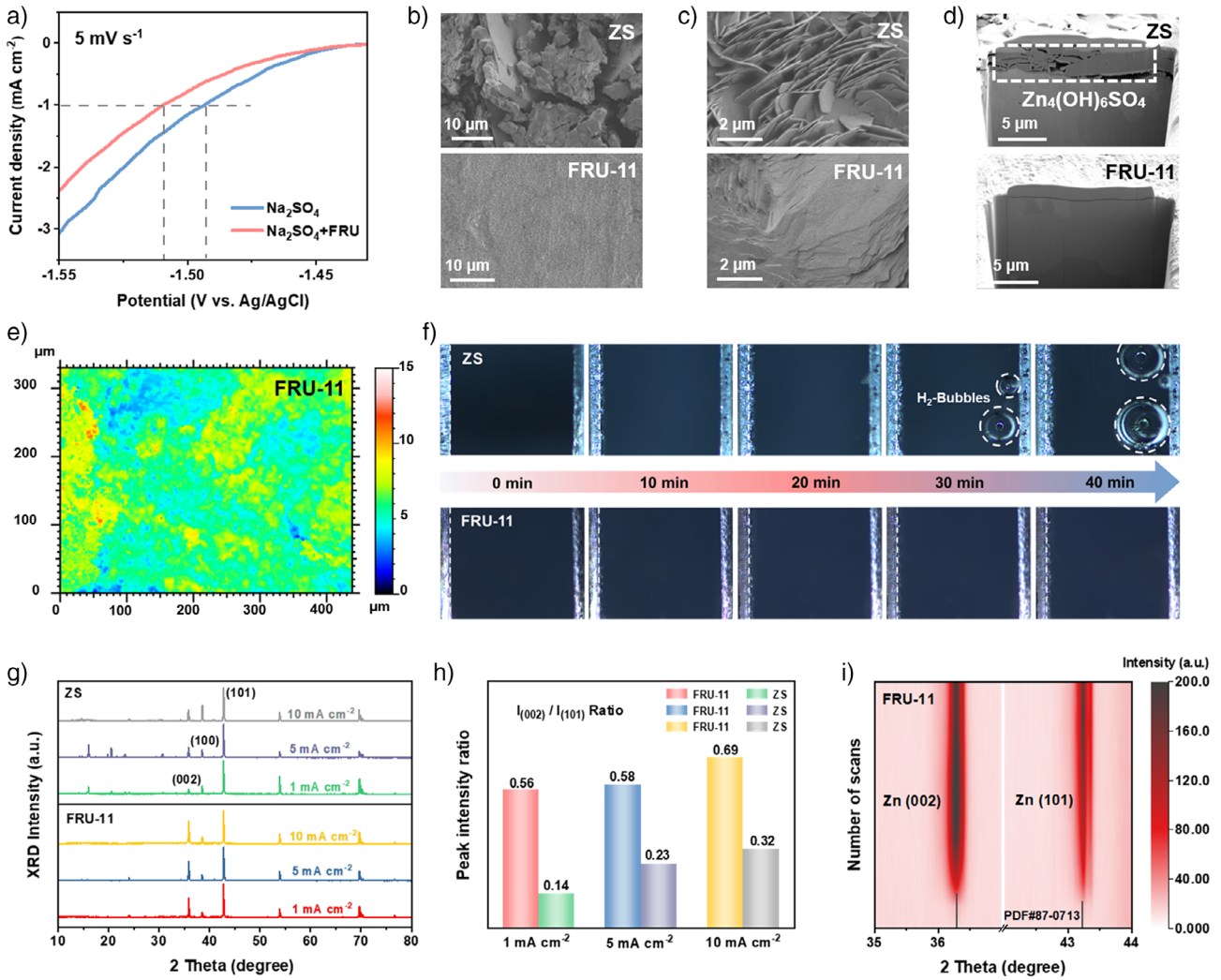

Figure 6. Morphological evolution and crystallographic orientation of Zn deposition. a) LSV curves tested in a three-electrode system. b) SEM images of Zn foil after soaking in ZS and FRU-11 electrolytes for 15 days. c) SEM and d) FIB-SEM images of zinc anodes after 100 cycles at 0.5 mA cm^{-2} in Zn//Zn symmetric cells with ZS and FRU-11 electrolytes. e) 3D LCSM images of zinc anode after 100 cycles in FRU-11. f) In situ optical microscopy images of Zn plating process in ZS and FRU-11 electrolytes at 5 mA cm^{-2}. g) XRD patterns of zinc anodes after being deposited at various current densities for 2 h in ZS and FRU-11 electrolytes and h) corresponding Zn(002)/(101) peak intensity ratios. i) In situ XRD patterns of zinc anode during continuous discharging at 6 mA cm^{-2} for 6 h in FRU-11.

ion beam scanning electron microscopy (FIB-SEM) cross-sectional images (Figures 6d and S39) and cross-sectional SEM images (Figure S40) further confirmed that the zinc deposition layer in ZS was loose and irregular, with dendrite fragments and byproducts [$Zn_4(OH)_6SO_4$].[81,82] In contrast, a uniform and dense deposition layer was formed in FRU-11.

Laser confocal scanning microscopy (LCSM) images further confirmed the effective inhibition of dendrite growth by FRU-11. The roughness of zinc anode using FRU-11 was maintained at less than 5 μm, suggesting a uniform and smooth surface (Figure 6e). Conversely, zinc anode with ZS exhibited a significant number of needle-like dendrites, with roughness reaching 40 μm (Figure S41).[83,84] In situ optical microscopy was employed to observe the Zn^{2+} electroplating process at a current density of 5 mA cm^{-2} (Figure 6f). In ZS, nonuniform nucleation sites appeared within only 10 min, and dendrites expanded over time, accompanied by significant bubble formation. The zinc anode in FRU-11 maintained a smooth and dense deposition morphology throughout the experiment, and no dendrite was formed even after 40 min of deposition.[85] The crystallographic orientation of the deposited zinc was further investigated by X-ray diffraction (XRD) (Figure 6g). After 2 h of deposition at various current densities, a significant amount of byproduct (5°–30°) was generated in ZS, and no preferred crystallographic orientation of zinc was observed. In contrast, FRU-11 guided the preferential growth of zinc along the (002) plane, and this preferred orientation was enhanced with increasing current density (Figure 6h). Almost no byproducts were produced even after cycling (Figure S42a).[86,87] In situ XRD also confirmed the effective regulation of zinc deposition orientation by FRU-11 (Figures 6i and S42b). After 6 h of continuous plating at 6 mA cm^{-2}, the peak intensity of the Zn(002) plane in FRU-11 was significantly stronger than that in ZS. A uniform and dense

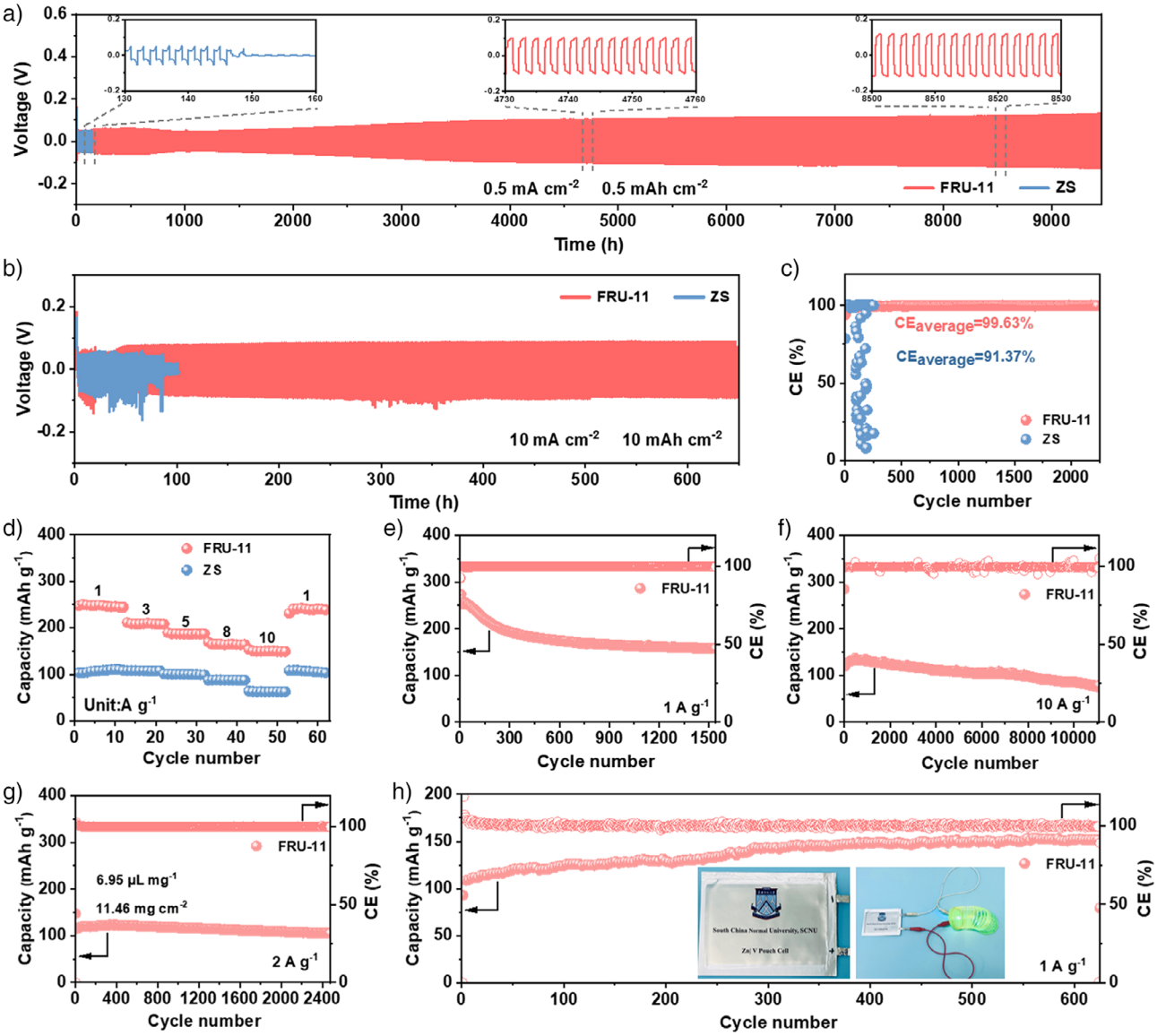

Figure 7. Battery performance. a) Long cycle performance of Zn//Zn symmetric cells with FRU-11 electrolyte at 0.5 mA cm^{-2} and 0.5 mAh cm^{-2}. b) Long cycle performance of Zn//Zn symmetric cells with FRU-11 electrolyte at 10 mA cm^{-2} and 10 mAh cm^{-2}. c) CE of Zn//Cu asymmetric cells. d) Rate capability of Zn//NVO full cells with ZS and FRU-11 electrolytes at various current densities. e) Cycling performance of Zn//NVO full cells with FRU-11 electrolyte at 1 A g^{-1}. f) Cycling performance of Zn//NVO full cells with FRU-11 electrolyte at 10 A g^{-1}. g) Cycling stability of Zn//NVO cells with FRU-11 electrolyte under lean electrolyte and high mass loading conditions at 2 A g^{-1}. h) Cycling performance of Zn//NVO pouch cell assembled with FRU-11 electrolyte at 1 A g^{-1}.

deposition, free of dendrites and side reactions was achieved by FRU-11 through effective regulation of Zn^{2+} adsorption, migration, and nucleation processes.

Electrochemical Performance of AZIBs

The high reversibility of zinc anode with FRU electrolyte was verified by long cycle tests in Zn//Zn symmetric cells and Zn//Cu asymmetric cells. The performance of FRU electrolytes with different $ZnSO_4$/FRU ratios was compared in Zn//Zn symmetric cells (Figure S43), confirming that FRU could significantly improve the reversibility of zinc deposition/stripping at any ratio. Notably, FRU outperformed other sugar additives in cycling stability, as quantitatively compared in Table S4.[38,49,58,88–91] In particular, an ultralong cycle life of over 9500 h was achieved with the FRU-11-based cell at a current density of 0.5 mA cm^{-2} (0.5 mAh cm^{-2}) (Figures 7a, S43, and 44). In contrast, the cell with ZS failed after only 145 h due to the severe interfacial side reactions and dendrite growth. Moreover, at a high current density of 10 mA cm^{-2} (10 mAh cm^{-2}), FRU-11 enabled a long cycle life of 650 h for the Zn//Zn symmetric cell (Figure 7b). Although voltage fluctuations were observed within the initial 50 h, which may be related to the dynamic SEI optimization process, FRU-11 still exhibited excellent cycling stability (Figure S45). The superior performance of FRU-11 was also demonstrated in Zn//Cu asymmetric cells

(Figures 7c and S46). At a current density of 0.5 mA cm^{-2}, the Zn^{2+} deposition/stripping process demonstrated a coulombic efficiency (CE) of 99.63% for over 2250 cycles, whereas the ZS electrolyte exhibited a significantly lower CE of 91.37% and experienced failure after merely several dozen cycles.

The effect of FRU-11 on electrochemical performance of full cell was explored based on Zn//NVO cell assembled with NVO positive electrode (NaV_3O_8 $1.5H_2O$) and Zn metal negative electrode. SEM and XRD characterizations confirmed the successful synthesis of the NVO cathode material (Figures S47 and 48). The electrolyte significantly influenced the intercalation/deintercalation behavior of Zn^{2+} in the NVO material. At scan rates from 0.2 to 1.0 mV s^{-1}, the CV curves of FRU-11 exhibited narrower redox peak voltage separations compared to ZS (Figure S49),[85] which was attributed to the enhanced reaction kinetics and reduced cell polarization facilitated by FRU-11. FRU-11 provided Zn//NVO full cells with excellent rate capability and cycling stability. High capacities of 245, 211, 189, 165, and 150 mAh g^{-1} were achieved at current densities ranging from 1 to 10 A g^{-1}, respectively (Figure 7d). The capacity quickly recovered to 242 mAh g^{-1} when the current density was returned to 1 A g^{-1}, demonstrating remarkable capacity retention. In contrast, the capacity of ZS-based cells remained consistently lower, limited by side reactions and other factors. With FRU-11, the cell retained a reversible capacity of 154 mAh g^{-1} after 1540 cycles at a current density of 1 A g^{-1}, with a CE approaching 100% (Figure 7e). Even under the more challenging conditions of a high current density of 10 A g^{-1}, a long cycle life exceeding 11 100 cycles was achieved (Figure 7f), highlighting its outstanding fast charging and discharging capabilities. Targeting practical applications, the Zn//NVO full cells exhibited outstanding cycling stability even under demanding conditions of high mass loading (11.46 mg cm^{-2}) and lean electrolyte usage (FRU-11, 6.95 μL mg^{-1}). Stable cycling for 2480 cycles was achieved at a current density of 2 A g^{-1}, with a capacity retention of 83.92% (Figure 7g). More importantly, FRU-11 also performed exceptionally well in pouch cells. A capacity retention of 100% was maintained after 600 cycles at 1 A g^{-1}, with a reversible capacity of 150 mAh g^{-1}. The pouch cell was also able to steadily power a rainbow circle (Figure 7h), demonstrating the feasibility of FRU-11 for commercial applications of low-cost, high-safety zinc-ion batteries.

Conclusions

In summary, by employing circular and linear sugar molecules as model additives, the relationship between molecular structure and desolvation behavior was established through combined experimental and theoretical approaches, systematically revealing that molecular size, steric configuration, and electronic structure are key design criteria for achieving fast interface kinetics. Among the four sugars, circular FRU with small size, delocalized electronic structure, and quasi-planar adsorption configuration exhibited the lowest desolvation energy and optimal performance under high current density and low temperature. Crucially, FRU's unique molecular structure facilitated multisite adsorption and a compact, thin EDL, effectively shortening Zn^{2+} diffusion paths, homogenizing Zn^{2+} flux, and accelerating interface kinetics via multisite desolvation. Moreover, FRU tailored Zn^{2+} solvation shells and induced organic–inorganic hybrid interfacial chemistry, suppressing parasitic reactions and dendrite growth, thereby enhancing zinc anode reversibility. Consequently, FRU-based electrolytes enabled Zn//Zn symmetric cells to achieve a lifespan exceeding 9500 h. Furthermore, under practical conditions (lean electrolyte: 6.95 μL mg^{-1}; high mass loading: 11.94 mg cm^{-2}), Zn//NVO full cells retained 83.92% capacity after 2480 cycles. This study provides critical guidelines for additive design and new perspectives for developing high-performance AZIB electrolytes.

Acknowledgements

This work was supported by the National Natural Science Foundation of China (Nos. 22379047 and 22409194), the Ningbo Yinzhou District Entrepreneurial and Innovative Team Project (X.W.), the Guangdong Provincial Regional Joint Fund for Basic and Applied Basic Research (No. 2022B1515120019), and the Outstanding Youth Project of the Guangdong Natural Science Foundation (No. 2021B1515020051). The authors acknowledge the support of the Energy Revolution S&T Program of Yulin Innovation Institute of Clean Energy (Grant No. YICE E411060316). The authors acknowledge the technical support provided by the Vacuum Interconnected Nanotech Workstation (Nano-X) at the Suzhou Institute of Nano-Tech and Nano-Bionics, Chinese Academy of Sciences.

Conflict of Interests

The authors declare no conflict of interest.

Data Availability Statement

The data that support the findings of this study are available from the corresponding author upon reasonable request.

Keywords: Aqueous zinc ion batteries · Circular additives · Dendrite-free deposition · Desolvation kinetics · Molecular engineering

[1] Y. Dai, R. Lu, C. Zhang, J. Li, Y. Yuan, Y. Mao, C. Ye, Z. Cai, J. Zhu, J. Li, R. Yu, L. Cui, S. Zhao, Q. An, G. He, G. I. N. Waterhouse, P. R. Shearing, Y. Ren, J. Lu, K. Amine, Z. Wang, L. Mai, *Nat. Catal.* **2024**, *7*, 776–784.
[2] Q. Ma, R. Gao, Y. Liu, H. Dou, Y. Zheng, T. Or, L. Yang, Q. Li, Q. Cu, R. Feng, Z. Zhang, Y. Nie, B. Ren, D. Luo, X. Wang, A. Yu, Z. Chen, *Adv. Mater.* **2022**, *34*, 2207344.
[3] C. Nie, G. Wang, D. Wang, M. Wang, X. Gao, Z. Bai, N. Wang, J. Yang, Z. Xing, S. Dou, *Adv. Energy Mater.* **2023**, *13*, 2300606.
[4] J. Wei, P. Zhang, J. Sun, Y. Liu, F. Li, H. Xu, R. Ye, Z. Tie, L. Sun, Z. Jin, *Chem. Soc. Rev.* **2024**, *53*, 10335–10369.

[5] Y. Zhu, G. Liang, X. Cui, X. Liu, H. Zhong, C. Zhi, Y. Yang, *Energy Environ. Sci.* **2024**, *17*, 369–385.
[6] Y. Li, B. Ping, J. Qu, J. Ren, C. Lin, J. Lei, J. Chen, J. Li, R. Liu, X. Long, X. Guo, D. Luo, Z. Chen, *Adv. Energy Mater.* **2025**, 2405804.
[7] J. Liu, C. Li, Q. Lv, D. Chen, J. Zhao, X. Xia, Z. Wu, J. Lai, L. Wang, *Adv. Energy Mater.* **2024**, *14*, 2401118.
[8] Y. Liu, Y. An, L. Wu, J. Sun, F. Xiong, H. Tang, S. Chen, Y. Guo, L. Zhang, Q. An, L. Mai, *ACS Nano* **2023**, *17*, 552–560.
[9] B. Luo, Y. Wang, S. Zheng, L. Sun, G. Duan, Z. Bao, Z. Ye, J. Huang, *Energy Storage Mater.* **2024**, *71*, 103661.
[10] L. Hong, J. Guan, Y. Tan, Y. Chen, Y.-S. Liu, W. Huang, C. Yu, Y. Zhou, J.-S. Chen, K.-X. Wang, *Energy Environ. Sci.* **2024**, *17*, 3157–3167.
[11] P. Wang, S. Liang, C. Chen, X. Xie, J. Chen, Z. Liu, Y. Tang, B. Lu, J. Zhou, *Adv. Mater.* **2022**, *34*, 2202733.
[12] K. Yang, H. Fu, Y. Duan, Z. Ma, D. Wang, B. Li, H. S. Park, D. Ho, *ACS Energy Lett.* **2024**, *9*, 209–217.
[13] Y. Geng, L. Pan, Z. Peng, Z. Sun, H. Lin, C. Mao, L. Wang, L. Dai, H. Liu, K. Pan, X. Wu, Q. Zhang, Z. He, *Energy Storage Mater.* **2022**, *51*, 733–755.
[14] K. Liu, M. Sun, S. Yang, G. Gan, S. Bu, A. Zhu, D. Lin, T. Zhang, C. Luan, C. Zhi, P. Wang, B. Huang, G. Hong, W. Zhang, *Adv. Energy Mater.* **2024**, *14*, 2401479.
[15] Y. Pan, Z. Zuo, Y. Jiao, P. Wu, *Adv. Mater.* **2024**, *36*, 2314144.
[16] M. Wang, J. Zhang, M. Wu, D. Yang, P. Sun, J. Sun, Z. Zhang, X. Chen, J. Ba, Y. Wang, J. Qiu, Y. Wei, *Adv. Funct. Mater.* **2024**, *34*, 2315757.
[17] L. Zhang, B. Zhang, T. Zhang, T. Li, T. Shi, W. Li, T. Shen, X. Huang, J. Xu, X. Zhang, Z. Wang, Y. Hou, *Adv. Funct. Mater.* **2021**, *31*, 2100186.
[18] H. Li, Y. Li, M. Liu, Z. Yang, Y. Gong, J. Qian, R. Zhang, Y. Bai, F. Wu, C. Wu, *Energy Environ. Sci.* **2025**, *18*, 2973–2984.
[19] S. Qin, J. Zhang, M. Xu, P. Xu, J. Zou, J. Li, D. Luo, Y. Zhang, H. Dou, Z. Chen, *Angew. Chem. Int. Ed.* **2024**, *63*, e202410422.
[20] T. Yan, S. Liu, J. Li, M. Tao, J. Liang, L. Du, Z. Cui, H. Song, *ACS Nano* **2024**, *18*, 3752–3762.
[21] Z. Zha, T. Sun, D. Li, T. Ma, W. Zhang, Z. Tao, *Energy Storage Mater.* **2024**, *64*, 103059.
[22] Y. Li, L. Liu, H. Zhang, H. Wang, Z. Sun, Z. Zhang, W. Pang, S. Omanovic, S. Sun, X. Chen, H. Song, *Adv. Funct. Mater.* **2025**, *35*, 2410855.
[23] T. Wei, L. Mo, Y. Ren, H. Zhang, M. Wang, Y. He, P. Tan, Z. Li, W. Chen, L. Hu, *Energy Storage Mater.* **2024**, *70*, 103525.
[24] Z. Xiao, X. Dai, J. Zhu, D. Liu, L. Liu, X. Liu, Y. Li, Z. Qian, R. Wang, *Adv. Funct. Mater.* **2025**, 2424860.
[25] D. Xie, H.-H. Liu, C. Liu, W.-Y. Diao, F.-Y. Tao, W.-B. Jiang, H.-Z. Sun, J.-W. Wang, H. Yu, W.-L. Li, X.-L. Wu, J.-P. Zhang, *Energy Storage Mater.* **2024**, *70*, 103524.
[26] M. Xu, B. Zhang, Y. Sang, D. Luo, R. Gao, Q. Ma, H. Dou, Z. Chen, *Energy Environ. Sci.* **2024**, *17*, 8966–8977.
[27] X. Gan, J. Tang, X. Wang, L. Gong, I. Zhitomirsky, L. Qie, K. Shi, *Energy Storage Mater.* **2023**, *59*, 102769.
[28] J. Huang, Y. Zhong, H. Fu, Y. Zhao, S. Li, Y. Xie, H. Zhang, B. Lu, L. Chen, S. Liang, J. Zhou, *Adv. Mater.* **2024**, *36*, 2406257.
[29] X. Yang, Y. Zhao, S. Lv, L. Zhong, C. Yue, S. Zhan, L. Zhao, C. Wang, X. Li, X. Liu, Z. Tang, C. Zhang, C. Zhi, H. Lv, *Energy Environ. Sci.* **2024**, *17*, 4758–4769.
[30] Z. Chen, W. Zhou, S. Zhao, X. Lou, S. Chen, *Adv. Energy Mater.* **2025**, *15*, 2404108.
[31] F. Cheng, X. Zhang, S. Wang, J. An, Y. Tong, X. Hou, H. Du, Y. Liu, Z. Wu, Y. Xue, Z. Fang, *Energy Storage Mater.* **2025**, *74*, 103933.
[32] L. Ding, L. Wang, J. Gao, T. Yan, H. Li, J. Mao, F. Song, S. Fedotov, L.-Y. Chang, N. Li, Y. Su, T. Liu, L. Zhang, *Adv. Funct. Mater.* **2023**, *33*, 2301648.
[33] N. Wang, X. Dong, B. Wang, Z. Guo, Z. Wang, R. Wang, X. Qiu, Y. Wang, *Angew. Chem. Int. Ed.* **2020**, *59*, 14577–14583.
[34] Y. Dong, H. Hu, P. Liang, L. Xue, X. Chai, F. Liu, M. Yu, F. Cheng, *Nat. Rev. Chem.* **2025**, *9*, 102–117.
[35] H. Lin, L. Zeng, C. Lin, J. Wu, H. He, C. Huang, W. Lai, P. Xiong, F. Xiao, Q. Qian, Q. Chen, J. Lu, *Energy Environ. Sci.* **2025**, *18*, 1282–1293.
[36] Y. Wang, T. Wang, Y. Mao, Z. Li, H. Yu, M. Su, K. Ye, D. Cao, K. Zhu, *Adv. Energy Mater.* **2024**, *14*, 2400353.
[37] Y. Xiong, W. Teng, Z. Zhao, S. Xu, Y. Ma, Y. Gong, D. Li, X. Wang, Y. Shen, Z. Shen, Y. Hu, *Energy Storage Mater.* **2025**, *74*, 103959.
[38] L. Zhou, R. Yang, S. Xu, X. Lei, Y. Zheng, J. Wen, F. Zhang, Y. Tang, *Angew. Chem. Int. Ed.* **2023**, *62*, e202307880.
[39] L. Geng, J. Meng, X. Wang, W. Wu, K. Han, M. Huang, C. Han, L. Wu, J. Li, L. Zhou, L. Mai, *Chem* **2025**, *11*, 102302.
[40] W. Ma, S. Wang, X. Wu, W. Liu, F. Yang, S. Liu, S. C. Jun, L. Dai, Z. He, Q. Zhang, *Energy Environ. Sci.* **2024**, *17*, 4819–4846.
[41] A. Wu, S. Zhang, Q. Li, W. Xue, C. Li, B. Xi, W. Mao, K. Bao, S. Xiong, *Adv. Energy Mater.* **2025**, *15*, 2404450.
[42] Z. Cui, D. Wang, J. Guo, Q. Nian, D. Ruan, J. Fan, J. Ma, L. Li, Q. Dong, X. Luo, Z. Wang, X. Ou, R. Cao, S. Jiao, X. Ren, *J. Am. Chem. Soc.* **2024**, *146*, 27644–27654.
[43] N. Hu, J. Tao, Y. Tan, H. Song, D. Huang, P. Liu, Z. Chen, X. Yin, J. Zhu, J. Xu, H. He, *Adv. Energy Mater.* **2024**, *14*, 2404018.
[44] Y. Ma, S.-P. Zhao, Y. Xu, L. Tang, Y. Zhang, Y.-L. Luo, C.-H. Li, *J. Mater. Chem. A* **2025**, *13*, 2884–2894.
[45] L. Zheng, H. Li, M. Gao, K. Huang, J. Wang, L. Su, L. Li, H. Lin, X. Gao, Z. Liu, H. Zhang, *Adv. Sci.* **2024**, *11*, 2407102.
[46] D.-Q. Cai, H. Cheng, J.-L. Yang, H. Liu, T. Xiao, X. Liu, M. Chen, H. J. Fan, *Energy Environ. Sci.* **2024**, *17*, 8349–8359.
[47] W. Guo, L. Xu, Y. Su, L. Zhao, Y. Ding, Y. Zou, G. Zheng, T. Cheng, J. Sun, *Angew. Chem. Int. Ed.* **2025**, *64*, e202417125.
[48] X. Liu, S. Wu, Z. Hao, L. Shang, M. Guo, J. Hou, S. Shao, H. Li, Y. Li, Y. Lu, K. Zhang, Z. Yan, J. Chen, *Angew. Chem. Int. Ed.* **2025**, *64*, e202416731.
[49] P. Sun, L. Ma, W. Zhou, M. Qiu, Z. Wang, D. Chao, W. Mai, *Angew. Chem. Int. Ed.* **2021**, *60*, 18247–18255.
[50] F. Bu, Y. Gao, W. Zhao, Q. Cao, Y. Deng, J. Chen, J. Pu, J. Yang, Y. Wang, N. Yang, T. Meng, X. Liu, C. Guan, *Angew. Chem. Int. Ed.* **2024**, *63*, e202318496.
[51] H. Wang, W. Ye, B. Yin, K. Wang, M. S. Riaz, B. B. Xie, Y. Zhong, Y. Hu, *Angew. Chem. Int. Ed.* **2023**, *62*, e202218872.
[52] Q. Li, D. Luo, Q. Ma, Z. Zheng, S. Li, Y. Xie, L. Xue, M. Lin, Y. Nie, G. Feng, H. Dou, J. Chen, X. Wang, Z. Chen, *Energy Environ. Sci.* **2025**, *18*, 1489–1501.
[53] S. Qin, J. Zhang, M. Xu, P. Xu, J. Zou, J. Li, D. Luo, Y. Zhang, H. Dou, Z. Chen, *Angew. Chem. Int. Ed.* **2024**, *63*, e202410422.
[54] X.-X. Zeng, S. Zhang, T. Long, Q.-Y. Zhao, H.-R. Wang, W. Ling, X.-W. Wu, A. Yu, Z. Chen, *Renewables* **2024**, *2*, 52–60.
[55] R. Chua, Y. Cai, P. Q. Lim, S. Kumar, R. Satish, W. Manalastas, Jr., H. Ren, V. Verma, S. Meng, S. A. Morris, P. Kidkhunthod, J. Bai, M. Srinivasan, *ACS Appl. Mater. Interfaces* **2020**, *12*, 22862–22872.
[56] Q. Hou, Y. Wu, S. Zhou, Y. Wei, J. Caro, H. Wang, *Angew. Chem. Int. Ed.* **2019**, *58*, 2–2.
[57] T. Sun, X. Yuan, K. Wang, S. Zheng, J. Shi, Q. Zhang, W. Cai, J. Liang, Z. Tao, *J. Mater. Chem. A* **2021**, *9*, 7042–7047.
[58] W. Chen, S. Guo, L. Qin, L. Li, X. Cao, J. Zhou, Z. Luo, G. Fang, S. Liang, *Adv. Funct. Mater.* **2022**, *32*, 2112609.
[59] Q. Zhang, K. Xia, Y. Ma, Y. Lu, L. Li, J. Liang, S. Chou, J. Chen, *ACS Energy Lett.* **2021**, *6*, 2704–2712.
[60] Y. Dong, L. Miao, G. Ma, S. Di, Y. Wang, L. Wang, J. Xu, N. Zhang, *Chem. Sci.* **2021**, *12*, 5843–5852.
[61] T. C. Li, Y. Lim, X. L. Li, S. Luo, C. Lin, D. Fang, S. Xia, Y. Wang, H. Y. Yang, *Adv. Energy Mater.* **2022**, *12*, 2103231.

[62] H. Dou, X. Wu, M. Xu, R. Feng, Q. Ma, D. Luo, K. Zong, X. Wang, Z. Chen, *Angew. Chem. Int. Ed.* **2024**, *63*, e202401974.
[63] J. Li, S. Qin, M. Xu, W. Wang, J. Zou, Y. Zhang, H. Dou, Z. Chen, *Adv. Funct. Mater.* **2024**, *34*, 2402186.
[64] Y. Xia, Z. Hong, L. Zhou, S. Chen, Z. Luo, S. Jin, Y. Huang, Y. Jiang, Y. Wu, *J. Energy Chem.* **2023**, *87*, 153–161.
[65] S. Fang, F. Wu, S. Zhao, M. Zarrabeitia, G.-T. Kim, J.-K. Kim, N. Zhou, S. Passerini, *Adv. Energy Mater.* **2023**, *13*, 2302577.
[66] X. Li, S. Wang, T. Wang, Z. Duan, Z. Huang, G. Liang, J. Fan, C. Yang, A. L. Rogach, C. Zhi, *Nano Energy* **2022**, *98*, 107278.
[67] L. Jiang, D. Li, X. Xie, D. Ji, L. Li, L. Li, Z. He, B. Lu, S. Liang, J. Zhou, *Energy Storage Mater.* **2023**, *62*, 102932.
[68] Z. Hu, F. Zhang, F. Wu, H. Wang, A. Zhou, Y. Chen, T. Xue, R. Chen, L. Li, *Energy Environ. Sci.* **2024**, *17*, 4794–4802.
[69] D. Li, Y. Tang, S. Liang, B. Lu, G. Chen, J. Zhou, *Energy Environ. Sci.* **2023**, *16*, 3381–3390.
[70] X. Lu, L. Tao, K. Qu, A. Amardeep, J. Liu, *Adv. Funct. Mater.* **2023**, *33*, 2211736.
[71] K. Wang, T. Qiu, L. Lin, H. Zhan, X.-X. Liu, X. Sun, *ACS Energy Lett.* **2024**, *9*, 1000–1007.
[72] X. Fang, C. Hu, X. Sun, H. Wang, J. Li, *Adv. Energy Mater.* **2024**, *14*, 2302499.
[73] P. Xu, M. Xu, J. Zhang, J. Zou, Y. Shi, D. Luo, D. Wang, H. Dou, Z. Chen, *Angew. Chem. Int. Ed.* **2024**, *63*, e202407909.
[74] J. Cao, D. Zhang, C. Gu, X. Wang, S. Wang, X. Zhang, J. Qin, Z.-S. Wu, *Adv. Energy Mater.* **2021**, *11*, 2101299.
[75] D. Wang, D. Lv, H. Liu, S. Zhang, C. Wang, C. Wang, J. Yang, Y. Qian, *Angew. Chem. Int. Ed.* **2022**, *61*, e202212839.
[76] J. Xiao, X. Zhang, H. Fan, Y. Zhao, Y. Su, H. Liu, X. Li, Y. Su, H. Yuan, T. Pan, Q. Lin, L. Pan, Y. Zhang, *Adv. Mater.* **2022**, *34*, e2203783.
[77] J. Zhang, Y. Wang, Z. Zhao, P. Li, G. Tang, W. Chen, Z. Peng, *Adv. Energy Mater.* **2024**, *14*, 2401560.
[78] X. Yu, Z. Li, X. Wu, H. Zhang, Q. Zhao, H. Liang, H. Wang, D. Chao, F. Wang, Y. Qiao, H. Zhou, S.-G. Sun, *Joule* **2023**, *7*, 1145–1175.
[79] R. Qin, Y. Wang, M. Zhang, Y. Wang, S. Ding, A. Song, H. Yi, L. Yang, Y. Song, Y. Cui, J. Liu, Z. Wang, S. Li, Q. Zhao, F. Pan, *Nano Energy* **2021**, *80*, 105478.
[80] C. Huang, J. Mao, S. Li, W. Zhang, X. Wang, Z. Shen, S. Zhang, J. Guo, Y. Xu, Y. Lu, J. Lu, *Adv. Funct. Mater.* **2024**, *34*, 2315855.
[81] X. Zeng, J. Mao, J. Hao, J. Liu, S. Liu, Z. Wang, Y. Wang, S. Zhang, T. Zheng, J. Liu, P. Rao, Z. Guo, *Adv. Mater.* **2021**, *33*, 2007416.
[82] H. Yang, Y. Yang, W. Yang, G. Wu, R. Zhu, *Energy Environ. Sci.* **2024**, *17*, 1975–1983.
[83] H. Yu, D. Chen, X. Ni, P. Qing, C. Yan, W. Wei, J. Ma, X. Ji, Y. Chen, L. Chen, *Energy Environ. Sci.* **2023**, *16*, 2684–2695.
[84] Q. Meng, Q. Bai, R. Zhao, P. Cao, G. Zhang, J. Wang, F. Su, X. Zhou, J. Yang, J. Tang, *Adv. Energy Mater.* **2023**, *13*, 2302828.
[85] Y. Li, J. Cheng, D. Zhao, X. Chen, G. Sun, S. Qiao, W. Zhang, Q. Zhu, *Energy Storage Mater.* **2023**, *63*, 102997.
[86] W. Xie, K. Zhu, W. Jiang, H. Yang, M. Ma, L. Zhao, W. Yang, *ACS Nano* **2024**, *18*, 21184–21197.
[87] D. Xu, X. Ren, H. Li, Y. Zhou, S. Chai, Y. Chen, H. Li, L. Bai, Z. Chang, A. Pan, H. Zhou, *Angew. Chem. Int. Ed.* **2024**, *63*, e202402833.
[88] Y. Cao, X. Tang, L. Li, H. Tu, Y. Hu, Y. Yu, S. Cheng, H. Lin, L. Zhang, J. Di, Y. Zhang, M. Liu, *Nano Res.* **2023**, *16*, 3839–3846.
[89] W. Guo, L. Xu, Y. Su, L. Zhao, Y. Ding, Y. Zou, G. Zheng, T. Cheng, J. Sun, *Angew. Chem. Int. Ed.* **2025**, *64*, e202417125.
[90] H. Li, Y. Ren, Y. Zhu, J. Tian, X. Sun, C. Sheng, P. He, S. Guo, H. Zhou, *Angew. Chem. Int. Ed.* **2023**, *62*, e202310143.
[91] M. Shi, C. Lei, H. Wang, P. Jiang, C. Xu, W. Yang, X. He, X. Liang, *Angew. Chem. Int. Ed.* **2024**, *63*, e202407261.

Manuscript received: March 06, 2025
Revised manuscript received: April 28, 2025
Accepted manuscript online: May 18, 2025
Version of record online: ■■, ■■

Research Article

Batteries

J. Yan, H. Dou*, M. Su, M. Xu, S. Liu, S. Qin, B. Zhang, K. Zong, L. Tan, X. Wang*, Z. Chen* — **e202505372**

Molecularly Engineered Circular Additive with Multisite Desolvation for High-Performance Zinc Ion Battery

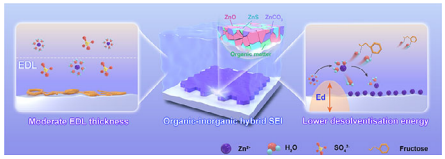

Fructose (FRU), based on its cyclic molecular framework, directionally assembles a moderate-thickness EDL at the zinc electrode interface through its nanoscale molecular configuration, quasi-planar adsorption orientation, and electron delocalization effects. This structure triggers the reconstruction of Zn^{2+} desolvation pathways via multisite synergistic effects, significantly reducing the desolvation energy barrier, thereby achieving ultrafast interfacial mass transfer kinetics and dendrite-free zinc deposition behavior.